Distinguishing NFW and Isothermal Density Profiles with Weak Gravitational Lensing

Ian Holst and Doyee Byun

May 8, 2018

Abstract

We examine the feasibility of distinguishing NFW and cored isothermal density profiles using weak gravitational lensing shear.

We model lenses in the two different profiles, as well as background galaxies to be lensed. Analyzing the simulated data of these lensed galaxies gives us insight into how we can distinguish the differences between the two profiles. This method is expected to be helpful in the analysis of real observation data in the future.

1 Introduction

Gravitational lensing allows us to investigate the matter density distributions of cosmic objects by observing the characteristic light distortions imparted on other objects in the background. The principle is applicable on a large range of scales, from all-sky mass maps based on cosmic microwave background shear, to studies of individual galaxies and clusters. In particular, by observing the coherent distortions of many background galaxies, the shear profile, and consequently the density profile of a foreground halo lens may be determined.

Two commonly used density profiles in the field are the isothermal profile and the Navarro-Frenk-White (NFW) profile. The NFW profile has been found to fit simulated dark matter halos very well [], while the isothermal profile results from an idealized isothermal collapse []. Both profiles extend to infinity

It is of great interest to determine the general forms of halo density profiles since this tells us about structure formation and the nature of dark matter [] Lensing offers one of the few ways to probe the distribution of all matter, not just baryonic matter. rotation curve present difficulties (https://arxiv.org/pdf/astro-ph/0201352.pdf)

In this paper, we will investigate the distinguishability of NFW and isothermal profiles given galaxy-galaxy lensing data The goal of this project is to devise a method to analyze lensed galaxy cluster data and find which density profile is more probable between the isothermal and NFW profiles. In order to do so, we generate simulated data sets and analyze them to find the more probable profiles they would fit into. This analysis method is expected to be usable in determining the characteristics of real observed data as well.

Outline: We start by introducing the general lensing characteristics of spherical density profiles, followed by the specifics for cored isothermal and NFW profiles. We then describe The results

1.1 Lensing by a spherical lens profile

Here we define our conventions for various lensing quantities, which mainly conform to those used by Dodelson [2017]. We use the thin lens approximation and assume spherical lens profiles. Consider such a spherically symmetric halo density profile $\rho(r)$ acting as a gravitational lens. This lens halo is located at an angular diameter distance D_L from the observer and we want to find out how it affects a source object behind it at an angular diameter distance D_S. Set the z axis to be along the line of sight, and use local cylindrical coordinates R, ϕ, and z. The projected surface density Σ at radius R on the projected plane is obtained by integrating the density over the entire z axis:

$$\Sigma(R) = \int_{-\infty}^{\infty} dz \ \rho(\sqrt{R^2 + z^2}) \tag{1}$$

A useful related measure in gravitational lensing is the average projected surface density within a radius R:

$$\overline{\Sigma}(R) = \frac{1}{\pi R^2} \int_0^{2\pi} d\phi \int_0^R dR' \ \Sigma(R')R' \tag{2}$$

The critical surface density is an important quantity that marks the typical boundary between what is considered strong and weak lensing:

$$\Sigma_{\text{crit}} = \frac{c^2}{4\pi G} \frac{D_S}{D_{SL}D_L} \tag{3}$$

D_S and D_L are calculated like normal angular diameter distances in a flat expanding universe: $D = \chi(z)/(1+z)$, where $\chi(z)$ is the comoving distance to redshift z. The redshift z of an object, such as a halo lens or a background galaxy, is typically easy to measure. Note that D_{SL} is nominally the distance from the source to the lens, but since it is an angular diameter distance, it is calculated as $D_{SL} = (\chi_S - \chi_L)/(1 + z_S)$.

All relevant angles in this problem are small, so we can assume that $R = D_L\theta$, where θ is the angular position on the observer's sky, with the halo center at the origin. This may be represented as the vector $\vec{\theta}$, but in the spherically symmetric case, the magnitude θ is sufficient. Thus we can easily change variables in all lensing quantities from R to θ.

We define the convergence κ at angular position θ as the ratio of surface density to critical surface density. Strong lensing phenomena such as arcs, rings, multiple images, and magnification are dominant when the convergence is greater than 1, or the projected surface density is greater than the critical surface density.

$$\kappa(\theta) = \frac{\Sigma(\theta)}{\Sigma_{\text{crit}}} \tag{4}$$

While the convergence determines how an object is uniformly scaled or magnified by a gravitational lens, another quantity, shear, describes the stretching of images along an axis. Shear is usually expressed as two components, γ_1 and γ_2. The tangential shear γ_t is the component of stretching in the $\hat{\phi}$ direction. It can be shown that for a spherical lens profile, the only component of shear γ should be the tangential shear, γ_t. For a spherical lens, tangential shear can be shown to be simply related to the convergence and average convergence [Dodelson, 2017]:

$$\gamma_t(\theta) = \overline{\kappa}(\theta) - \kappa(\theta) \tag{5}$$

2

The tangential shear is decomposed into two components, γ_1 and γ_2. γ_1 represents stretching along the θ_x and θ_y axes, and γ_2 represents stretching along the $\theta_y = \theta_x$ and $\theta_y = -\theta_x$ lines. They can be obtained through a relation with γ_t and the cylindrical azimuthal angle ϕ.

$$\gamma_1 = -\gamma_t \cos 2\phi$$
$$\gamma_2 = -\gamma_t \sin 2\phi \tag{6}$$

The shear magnitude, which is equal to tangential shear, also follows from trigonometric identities:

$$\gamma = \gamma_t = -\gamma_1 \cos 2\phi - \gamma_2 \sin 2\phi \tag{7}$$

Changes in object shapes due to lensing can be quantified using the ellipticity ϵ. This is most commonly used in weak lensing, where shape changes are best described by simple stretching. Ellipticity is defined using the semimajor axis a and semiminor axis b of an ellipse [Narayan and Bartelmann, 1996]:

$$\epsilon = \frac{a^2 - b^2}{a^2 + b^2} \tag{8}$$

Like shear, there are two components of ellipticity, ϵ_1 and ϵ_2, which are analogous to the shear components γ_1 and γ_2. The ellipticity that would be induced in an otherwise perfectly circular object is:

$$\epsilon_i = \frac{2\gamma_i/(1-\kappa)}{1 + \gamma^2/(1-\kappa)^2} \tag{9}$$

And there is an analogous ellipticity magnitude or tangential ellipticity:

$$\epsilon = -\epsilon_1 \cos 2\phi - \epsilon_2 \sin 2\phi \tag{10}$$

Gravitational lensing causes a deflection in the observed image position of background objects. If the true position of the object is $\vec{\beta}$ and it appears at position $\vec{\theta}$, then the deflection angle is defined:

$$\vec{\alpha}(\vec{\theta}) = \overline{\kappa}(\theta)\vec{\theta} \tag{11}$$

From this expression, it can be seen that deflection is most significant in the strong lensing regime, where $\kappa > 1$.

1.2 Cored Isothermal Sphere Profile

The cored isothermal sphere (CIS) profile is related to the singular isothermal sphere (SIS) profile, which is often used to describe halos and other collapsed astrophysical objects because of its simple formulation. Unlike the singular isothermal sphere, the cored isothermal sphere does not have a density singularity at its center due to a finite core radius r_c. The CIS density profile is defined

$$\rho_{\mathrm{CIS}}(r) = \frac{\sigma^2}{2\pi G(r^2 + r_c{}^2)}, \tag{12}$$

where σ^2 is the velocity dispersion of the halo [Chen, 2005, Shapiro et al., 1998]. Applying equation 1 and defining $\theta_c = r_c/D_L$, we get the projected surface density of the CIS profile:

$$\Sigma_{\mathrm{CIS}}(\theta) = \frac{\sigma^2}{2GD_L\sqrt{\theta^2 + \theta_c{}^2}} \tag{13}$$

3

The average surface density inside angular radius θ is derived using equation 2:

$$\overline{\Sigma}_{\text{CIS}}(\theta) = \frac{\sigma^2 \left(\sqrt{\theta^2 + \theta_c{}^2} - \theta_c \right)}{GD_L\theta^2} \tag{14}$$

The tangential shear follows from equation 5:

$$\gamma_{\text{CIS}}(\theta) = \frac{\sigma^2 \left(\sqrt{\theta^2 + \theta_c{}^2} - \theta_c \right)}{\Sigma_{\text{crit}}GD_L\theta^2} - \frac{\sigma^2}{2\Sigma_{\text{crit}}GD_L\sqrt{\theta^2 + \theta_c{}^2}} \tag{15}$$

The ellipticity equations, while not quite elegant, are trivial to calculate from the shear.

Although the total mass of the CIS profile diverges, we will use a common convention for quantifying the mass of the profile within a reasonable radius. We define r_{200} as the radius at which the average enclosed density of the profile is 200 times the critical density of the universe. The critical density ρ_{crit} depends on cosmological parameters such as the Hubble constant H_0. We choose to use the critical density at the current time $\rho_{\text{crit},0}$ for all halos regardless of their redshift. We assume a flat ΛCDM universe and use the Planck 2015 results for all cosmological calculations [Planck Collaboration et al., 2015].

We define M_{200} as the total mass enclosed within r_{200}:

$$M_{200} = 200\rho_{\text{crit}}\frac{4}{3}\pi r_{200}{}^3 \tag{16}$$

We also calculate M_{200} specifically for a CIS profile by integrating equation 12:

$$M_{200} = M_{\text{enc}}(r_{200}) = \frac{2\sigma^2}{G} \left(r_{200} - r_c \arctan\left(\frac{r_{200}}{r_c} \right) \right) \tag{17}$$

Solving for r_{200}:

$$r_{200} = \left(\frac{3M_{200}}{800\pi\rho_{\text{crit}}} \right)^{1/3} \tag{18}$$

We can now completely switch the CIS profile's dependence from σ^2 to M_{200} with equation 18 and solving for σ^2 from equation 17:

$$\sigma^2 = \frac{M_{200}G}{2\left(r_{200} - r_c \arctan\left(\frac{r_{200}}{r_c} \right) \right)} \tag{19}$$

Figure 1 shows the convergence, tangential shear, and ellipticity of a Milky Way-sized halo lens at redshift 0.3 for lensed objects at redshift 1.

1.3 Navarro-Frenk-White (NFW) Profile

$$\rho_{\text{NFW}}(r) = \frac{\rho_{\text{crit}}\delta_c}{(r/r_s)\left(1 + r/r_s\right)^2} \tag{20}$$

$$\Sigma_{\text{NFW}}(\theta) = \frac{2\rho_{\text{crit}}\delta_c D_L\theta_s}{(\theta/\theta_s)^2 - 1} \left(1 - \frac{2}{\sqrt{(\theta/\theta_s)^2 - 1}} \arctan\left(\sqrt{\frac{\theta/\theta_s - 1}{\theta/\theta_s + 1}} \right) \right) \tag{21}$$

$$\overline{\Sigma}_{\text{NFW}}(\theta) = \frac{4\rho_{\text{crit}}\delta_c D_L\theta_s}{(\theta/\theta_s)^2} \left(\frac{2}{\sqrt{(\theta/\theta_s)^2 - 1}} \arctan\left(\sqrt{\frac{\theta/\theta_s - 1}{\theta/\theta_s + 1}} \right) + \ln\left(\frac{\theta/\theta_s}{2} \right) \right) \tag{22}$$
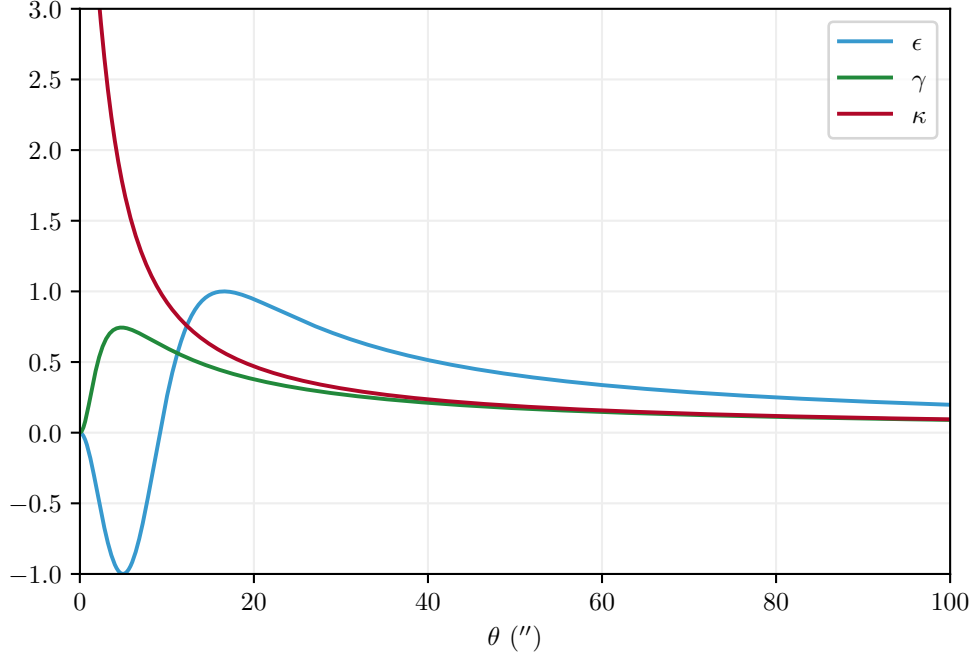
Figure 1: Lensing quantities for a CIS profile with $M_{200} = 10^{15} M_\odot$ and $r_c = 10$ kpc. $z_L = 0.3$ and $z_S = 1.0$.

Similar convention used by Bartelmann et al. [2001]

$$\gamma_{\mathrm{NFW}}(\theta) = \frac{\overline{\Sigma}_{\mathrm{NFW}}(\theta) - \Sigma_{\mathrm{NFW}}(\theta)}{\Sigma_{\mathrm{crit}}} \tag{23}$$

We can calculate ellipticities from tangential shear.

We switch the dependence to M_{200} and c with:

$$\delta_c = \frac{200}{3} \frac{c^3}{\ln(1+c) - c/(1+c)} \tag{24}$$

$$r_s = \frac{r_{200}}{c} \tag{25}$$

$$r_{200} = \left(\frac{3 M_{200}}{800 \pi \rho_{\mathrm{crit}}} \right)^{1/3} \tag{26}$$

$$c = \frac{r_{200}}{r_s} \tag{27}$$

2   Methods

2.1   Modelling of Foreground Lens and Background Galaxies

Based on the calculations shown above, we have modelled singular lenses corresponding to each density profile. Background galaxies have been generated via randomization of angular coordinates.
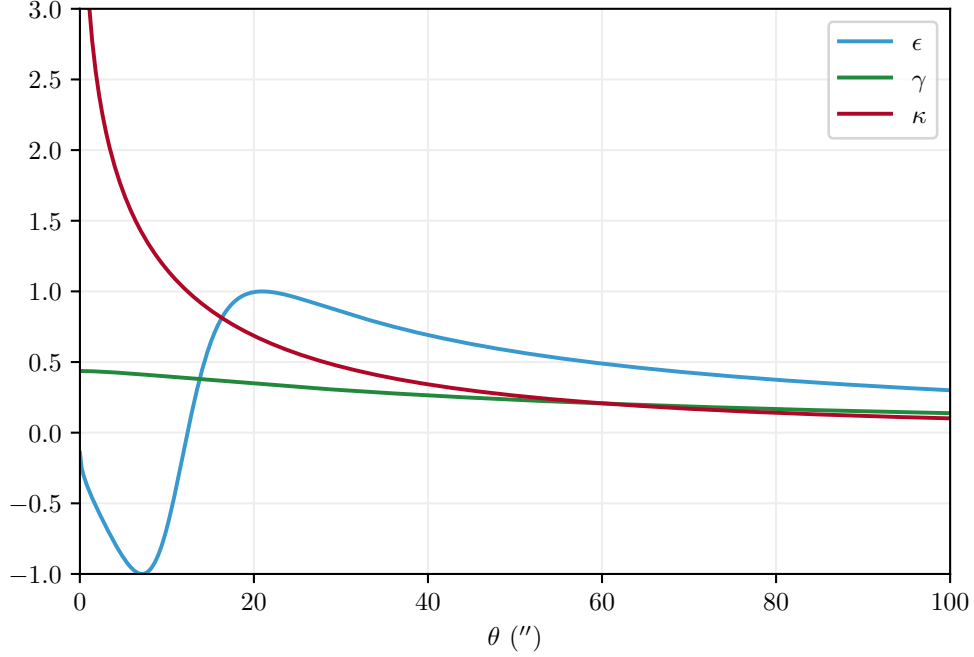
Figure 2: Lensing quantities for a NFW profile with $M_{200} = 10^{15} M_\odot$ and $c = 10$.

1. Consider single foreground lens halo with many background galaxies.

   - Start with one NFW halo, then maybe consider more tests.

2. Construct background galaxies:

   - Number density on sky: 50 galaxies/square arcminute (LSST, https://arxiv.org/pdf/1305.0793.pdf)

   - Intrinsic ellipticity drawn from Gaussian distribution with $\mu = 0, \sigma = 0.2$ (consistent with https://arxiv.org/pdf/1509.05058.pdf)

   - Assume they are all that the same distance D_S since this can be determined by redshift (neglecting some noise)

   - Apply shear and deflection angles to background galaxies to get simulated data: N sets of ϵ_1, ϵ_2, θ_1, θ_2

3. Recommended values:

   - $z_L = 0.3$ (bullet cluster)

   - $z_S = 1.0$ (Hubble Deep Field) (also consistent with https://arxiv.org/pdf/1509.05058.pdf) we use the planck 2015 results

   - $M_{halo} = 10^{15} M_\odot$

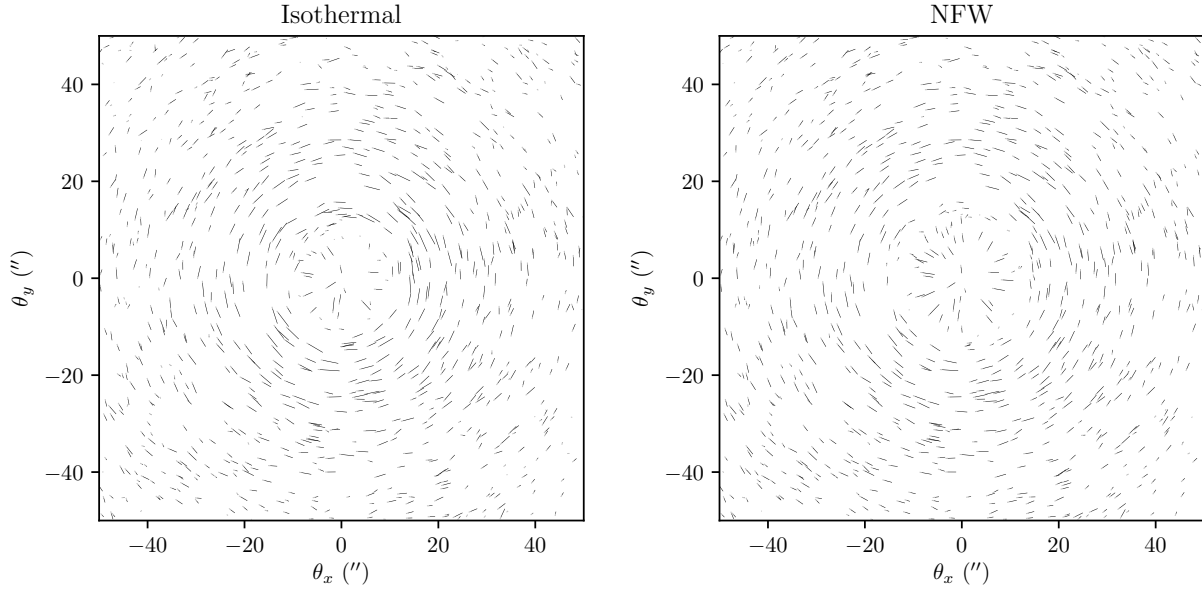Estimating ellipticity has well-documented issues [cite] due to noise and PSF

Figure 3: plots

2.2 Data Analysis and Density Profile Determination

1. Bin galaxies in annuli by θ value (use log bins for theta)

2. Calculate mean and standard deviation of ellipticity

3. Attempt to fit both NFW and isothermal profiles, see if the fit is distinguishable

3 Results

4 Conclusions

Like (COMPARISONS BETWEEN ISOTHERMAL AND NFW MASS PROFILES FOR STRONG-LENSING GALAXY CLUSTERS), we find that the strong lensing regime provides the most But also, weak lensing can in fact provide sufficient distinguishability

has been applied to observations before https://arxiv.org/pdf/astro-ph/9602053.pdf but not in the context of comparing density profiles using for strong and weak but this is highly dependent on good data

http://iopscience.iop.org/article/10.1086/590049/pdf looked at NFW vs isothermal in strong lensing with a focus on arcs, and found differing levels of distinguishibility for different lenses.

https://arxiv.org/pdf/1101.0650.pdf - our results don't match

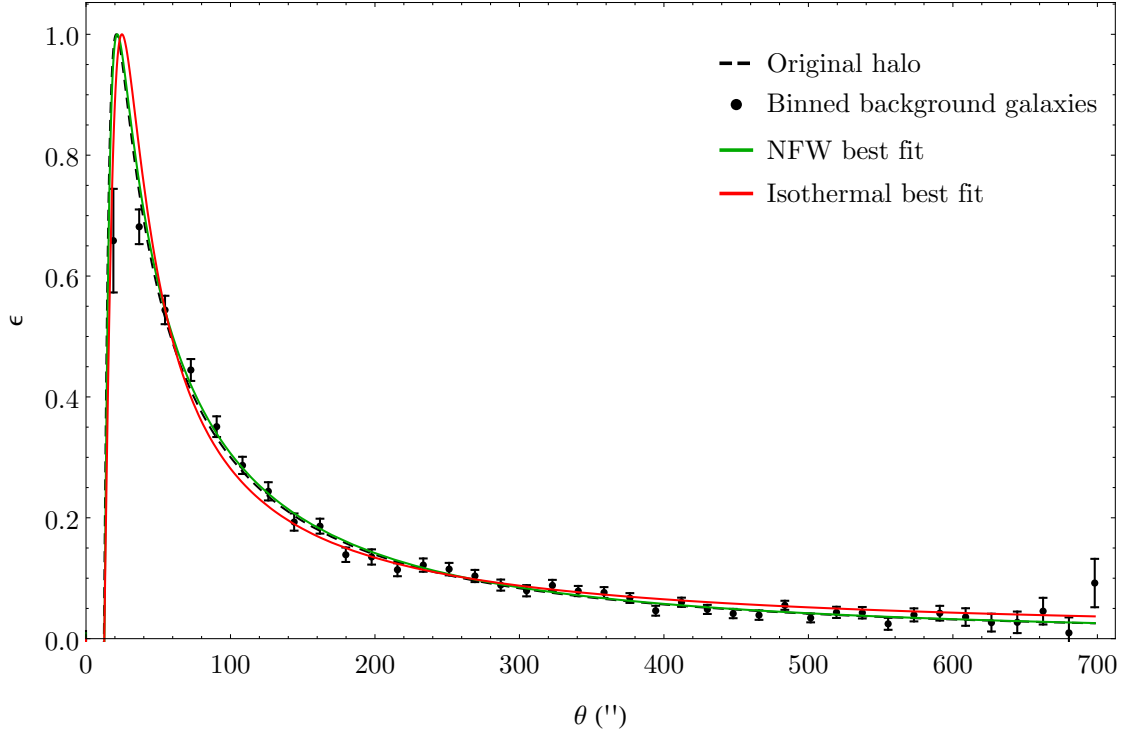ignore cosmic shear (https://journals.aps.org/prd/pdf/10.1103/PhysRevD.70.023008)

Figure 4: plots

From our data analysis, we were able to find the more probable density profile of a simulated data set. Since the simulated data is based on the NFW and isothermal profile models, we were able to decisively distinguish between the two. When analyzing real observed data, we expect the probability ratios to be relatively more even. Future goals include the use of these methods to analyze observed data of galaxy clusters to find the density profile of their lenses.

References

M. Bartelmann, L. J. King, and P. Schneider. Weak-lensing halo numbers and dark-matter profiles. *A&A*, 378(2):361–369, nov 2001. ISSN 0004-6361. doi: 10.1051/0004-6361:20011199. URL http://www.edpsciences.org/10.1051/0004-6361:20011199.

Da-ming Chen. Nonsingular Density Profiles of Dark Matter Halos and Strong Gravitational Lensing. *ApJ*, 629(1):23–28, aug 2005. ISSN 0004-637X. doi: 10.1086/431577. URL http://iopscience.iop.org/article/10.1086/431577/pdf http://stacks.iop.org/0004-637X/629/i=1/a=23.

S Dodelson. *Gravitational Lensing*. Cambridge University Press, jun 2017.

Ramesh Narayan and Matthias Bartelmann. Lectures on Gravitational Lensing. 1996. URL http://arxiv.org/abs/astro-ph/9606001.

Planck Collaboration, P. A. R. Ade, N. Aghanim, M. Arnaud, M. Ashdown, J. Aumont, C. Baccigalupi,

A. J. Banday, R. B. Barreiro, J. G. Bartlett, N. Bartolo, E. Battaner, R. Battye, K. Benabed, A. Benoit, A. Benoit-Levy, J. P. Bernard, M. Bersanelli, P. Bielewicz, J. J. Bock, A. Bonaldi, L. Bonavera, J. R. Bond, J. Borrill, F. R. Bouchet, F. Boulanger, M. Bucher, C. Burigana, R. C. Butler, E. Calabrese, J. F. Cardoso, A. Catalano, A. Challinor, A. Chamballu, R. R. Chary, H. C. Chiang, J. Chluba, P. R. Christensen, S. Church, D. L. Clements, S. Colombi, L. P. L. Colombo, C. Combet, A. Coulais, B. P. Crill, A. Curto, F. Cuttaia, L. Danese, R. D. Davies, R. J. Davis, P. de Bernardis, A. de Rosa, G. de Zotti, J. Delabrouille, F. X. Desert, E. Di Valentino, C. Dickinson, J. M. Diego, K. Dolag, H. Dole, S. Donzelli, O. Dore, M. Douspis, A. Ducout, J. Dunkley, X. Dupac, G. Efstathiou, F. Elsner, T. A. Ensslin, H. K. Eriksen, M. Farhang, J. Fergusson, F. Finelli, O. Forni, M. Frailis, A. A. Fraisse, E. Franceschi, A. Frejsel, S. Galeotta, S. Galli, K. Ganga, C. Gauthier, M. Gerbino, T. Ghosh, M. Giard, Y. Giraud-Heraud, E. Giusarma, E. Gjerlow, J. Gonzalez-Nuevo, K. M. Gorski, S. Gratton, A. Gregorio, A. Gruppuso, J. E. Gudmundsson, J. Hamann, F. K. Hansen, D. Hanson, D. L. Harrison, G. Helou, S. Henrot-Versille, C. Hernandez-Monteagudo, D. Herranz, S. R. Hildebrandt, E. Hivon, M. Hobson, W. A. Holmes, A. Hornstrup, W. Hovest, Z. Huang, K. M. Huffenberger, G. Hurier, A. H. Jaffe, T. R. Jaffe, W. C. Jones, M. Juvela, E. Keihanen, R. Keskitalo, T. S. Kisner, R. Kneissl, J. Knoche, L. Knox, M. Kunz, H. Kurki-Suonio, G. Lagache, A. Lahteenmaki, J. M. Lamarre, A. Lasenby, M. Lattanzi, C. R. Lawrence, J. P. Leahy, R. Leonardi, J. Lesgourgues, F. Levrier, A. Lewis, M. Liguori, P. B. Lilje, M. Linden-Vornle, M. Lopez-Caniego, P. M. Lubin, J. F. Macias-Perez, G. Maggio, D. Maino, N. Mandolesi, A. Mangilli, A. Marchini, P. G. Martin, M. Martinelli, E. Martinez-Gonzalez, S. Masi, S. Matarrese, P. Mazzotta, P. McGehee, P. R. Meinhold, A. Melchiorri, J. B. Melin, L. Mendes, A. Mennella, M. Migliaccio, M. Millea, S. Mitra, M. A. Miville-Deschenes, A. Moneti, L. Montier, G. Morgante, D. Mortlock, A. Moss, D. Munshi, J. A. Murphy, P. Naselsky, F. Nati, P. Natoli, C. B. Netterfield, H. U. Norgaard-Nielsen, F. Noviello, D. Novikov, I. Novikov, C. A. Oxborrow, F. Paci, L. Pagano, F. Pajot, R. Paladini, D. Paoletti, B. Partridge, F. Pasian, G. Patanchon, T. J. Pearson, O. Perdereau, L. Perotto, F. Perrotta, V. Pettorino, F. Piacentini, M. Piat, E. Pierpaoli, D. Pietrobon, S. Plaszczynski, E. Pointecouteau, G. Polenta, L. Popa, G. W. Pratt, G. Prezeau, S. Prunet, J. L. Puget, J. P. Rachen, W. T. Reach, R. Rebolo, M. Reinecke, M. Remazeilles, C. Renault, A. Renzi, I. Ristorcelli, G. Rocha, C. Rosset, M. Rossetti, G. Roudier, B. Rouille D'Orfeuil, M. Rowan-Robinson, J. A. Rubino-Martin, B. Rusholme, N. Said, V. Salvatelli, L. Salvati, M. Sandri, D. Santos, M. Savelainen, G. Savini, D. Scott, M. D. Seiffert, P. Serra, E. P. S. Shellard, L. D. Spencer, M. Spinelli, V. Stolyarov, R. Stompor, R. Sudiwala, R. Sunyaev, D. Sutton, A. S. Suur-Uski, J. F. Sygnet, J. A. Tauber, L. Terenzi, L. Toffolatti, M. Tomasi, M. Tristram, T. Trombetti, M. Tucci, J. Tuovinen, M. Turler, G. Umana, L. Valenziano, J. Valiviita, B. Van Tent, P. Vielva, F. Villa, L. A. Wade, B. D. Wandelt, I. K. Wehus, M. White, S. D. M. White, A. Wilkinson, D. Yvon, A. Zacchei, and A. Zonca. Planck 2015 results. XIII. Cosmological parameters. *A&A*, 594:A13, feb 2015. ISSN 0004-6361. doi: 10.1051/0004-6361/201525830. URL http://arxiv.org/abs/1502.01589%0Ahttp://dx.doi.org/10.1051/0004-6361/201525830 http://www.aanda.org/10.1051/0004-6361/201525830 http://arxiv.org/abs/1502.01589 http://dx.doi.org/10.1051/0004-6361/201525830.

Paul R. Shapiro, Ilian T. Iliev, and Alejandro C. Raga. A model for the postcollapse equilibrium of cosmological structure: truncated isothermal spheres from top-hat density perturbations. 224(December):29, 1998. ISSN 0035-8711. doi: 10.1046/j.1365-8711.1999.02609.x. URL http://arxiv.org/abs/astro-ph/9810164.